Supporting Information

CoSe-C@C Core-Shell Structure with Stable Potassium Storage Performance Realized by Effective Solid Electrolyte Interphase Layer

Xin Gu,*[a] Li Zhang,[a] Wenchao Zhang,*[bd] Sailin Liu,[d] Sheng Wen,[a] Xinning Mao,[a] Pengcheng Dai,[a] Liangjun Li,[a] Dandan Liu,[a] Xuebo Zhao *[a] and Zaiping Guo [cd]

[a] College of New Energy, State Key Laboratory of Heavy Oil Processing, China University of Petroleum (East China), Qingdao 266580, P. R. China. E-mail: guxin@upc.edu.cn; zhaoxuebo@upc.edu.cn

[b] Institute of Environmental Engineering, School of Metallurgy and Environment, Central South University, Changsha, Hunan 410083, China. E-mail: wz990@uowmail.edu.au

[c] School of Chemical Engineering & Advanced Materials, The University of Adelaide, Adelaide, SA 5005, Australia

[d] Institute for Superconducting and Electronic Materials, University of Wollongong, Wollongong, NSW 2522, Australia.

EXPERIMENTAL SECTION

Synthesis of ZIF-67 nanocubes. Firstly, 1.16 g Co(NO$_3$)$_2$·6H$_2$O and 0.02 g cetyltrimethylammonium bromide (CTAB) were dissolved in 40 mL deionized water. 18 g of 2-methylimidazole were dissolved in 280 mL deionized water. Then, the two solutions were mixed quickly and stirred for 20 min at room temperature. Finally, the ZIF-67 nanocubes were collected by centrifuging, washing with anhydrous ethanol three times, and drying under vacuum at 80 ^{o}C for 12 h.

Synthesis of ZIF-67@RF core-shell nanocubes. 0.4 g of the as-prepared ZIF-67 nanocubes was first dispersed in a mixed solution of ethanol (12 mL) and deionized water (28 mL) by ultrasonication. Second, 0.46 g CTAB, 0.07 g resorcinol, and 0.2 mL ammonium hydroxide were added into the above suspension and stirred for 30 min. Third, 0.12 mL formaldehyde was slowly added, followed by stirring at room temperature for 8 h. Finally, the resorcinol-formaldehyde (RF) resin coated ZIF-67 core-shell nanocubes (ZIF-67@RF) were obtained by filtering, washing with deionized water and ethanol, and drying under vacuum at 80 ^{o}C for 12 h. If the polymerization time was shortened to 1 h, ZIF-67@RF-1 showing thinner RF layer than ZIF-67@RF was obtained. ZIF-67@RF-2 with thicker RF layer than ZIF-67@RF was prepared by using 0.2 g ZIF-67 nanocubes as raw material under the same conditions.

Synthesis of CoSe-C@C core-shell nanocubes. The as-synthesized ZIF-67@RF and selenium powder in a mass ratio of 1:1 were mixed and fully ground in an agate mortar for 10 min. The CoSe-C@C core-shell nanocubes were produced by annealing the mixture at

800 °C for 2 h with a heating rate of 2 °C min^{-1} in flowing N_2 gas. For comparison, CoSe-C@C-1 and CoSe-C@C-2 were prepared by using ZIF-67@RF-1 and ZIF-67@RF-2 as precursors at the same procedure. CoSe-C@C-700 and CoSe-C@C-900 were obtained by the selenization of ZIF-67@RF precursor at 700 and 900 °C, respectively. The CoSe-C composite without additional carbon coating was directly synthesized by annealing a mixture of ZIF-67 and selenium powder under the same conditions.

Material characterizations. X-ray diffraction patterns were acquired on an X-ray diffractometer (Bruker D8 Advance). Raman spectra were obtained on a Raman spectrometer (NEXUS 670, 632 nm). The C content in the CoSe-based products was determined by thermogravimetric analysis (SDTA851, Mettler Toledo TGA) at a ramp rate of 10 °C min^{-1} in air. N_2 sorption measurements were performed at 77 K on a Quadrasorb SI. Nonlocal Density Functional Theory and the Brunauer-Emmett-Teller method were applied to evaluate the pore structure and surface area of the CoSe-based products. SEM images were collected with a scanning electron microscope (JSM-7500F). TEM images and EDS element mapping images were obtained using a transmission electron microscope (JEM-2100F). X-ray photoelectron spectroscopy measurements were performed on an X-ray photoelectron spectrometer (250X, ESCALAB).

Electrochemical measurements. The working electrodes were made from the active material, Super P, and sodium carboxymethyl cellulose (mass ratio = 70:15:15). The mass loading of active material was about 0.8-1.0 mg cm^{-2}. K half cells were assembled by using potassium foil as counter electrode, 1 M KFSI in EC/DEC or 0.8 M KPF_6 in EC/DEC (volume ratio of EC to

DEC, 1:1) as electrolyte, and glass fibre (Whatman GF/D) as separator. Galvanostatic discharge/charge measurements were conducted at current densities of 0.2 to 10 A g^{-1} in the potential range of 0.01-3.0 V (vs. K/K$^+$) on a battery cycler (LAND CT-2001A).

Galvanostatic intermittent titration technique (GITT) measurements were performed by alternating the cycling at 50 mA g^{-1} for 20 min with a rest interval of 2 h, after 10 activating cycles at 50 mA g^{-1}. The potential change during each relaxation period represents the overpotential at the corresponding discharge/charge state. As the cell voltage is linearly proportional to $\tau^{1/2}$ (Fig. S13b), where τ is the current pulse time, the K$^+$ diffusion coefficient (D_{K+}) in CoSe-C@C electrode can be determined by Fick's second law with the simplified equation:

$$D_{K^+} = \frac{4}{\pi\tau}\left(\frac{m_B V_M}{M_B S}\right)^2 \left(\frac{\Delta E_S}{\Delta E_\tau}\right)^2 \left(\tau \ll L^2/D_{K^+}\right)$$

where m_B is the mass of the electrode material, V_M is the molar volume of the electrode material, M_B is the molar mass of the electrode material, S is the geometric area of the electrode, L is the average thickness of the electrode, and ΔE_S and ΔE_τ in a single GITT process are shown in Fig. S11a.

Cyclic voltammetry (CV) measurements were carried out at scan rates of 0.2 to 1.0 mV s^{-1} in the potential range of 0.01-3.0 V (vs. K/K$^+$) on an electrochemical workstation (CHI760E, China). CV curves of CoSe-based electrodes in both the KFSI and the KPF$_6$ electrolytes were used to quantitatively analyse the contributions of capacitive K storage and diffusion-controlled K storage. Generally, a peak current (i) at different scan rates (v) obeys the formula: $i = av^b$, where a and b are constants. The b value can be calculated by plotting log(i) versus log(v). Qualitatively, a b

value of 1 indicates surface-driven capacitive behaviour, while a b value of 0.5 reveals a diffusion-controlled intercalation process. Quantitatively, the current response (i) at a fixed potential (V) can be separated into a surface-dependent capacitive process (proportional to v) and a diffusion-controlled intercalation process (proportional to $v^{1/2}$) by the formula: $i_{(V)} = k_1 v + k_2 v^{1/2}$, in which k_1 and k_2 are constants. The values of k_1 and k_2 can be obtained by plotting $i_{(V)}/v^{1/2}$ versus $v^{1/2}$.

Theoretical calculations. All calculations were performed with the Materials Studio using the density functional theory (DFT). The electron exchange and correlation interaction were processed by the Perdew–Burke–Ernzerhof (PBE) pseudopotentials within the generalized gradient approximation (GGA). After checking for convergence, 300 eV was chosen as the cut-off energy of the plane-wave basis for the Kohn–Sham states. For geometry optimization, the following convergent tolerances in Dmol3 package were set: the energy, the maximum allowed force and the maximum displacement were 2×10^{-5} hartree (1 hartree=27.21 eV), 0.004 hartree Å^{-1} and 0.005 Å, respectively.
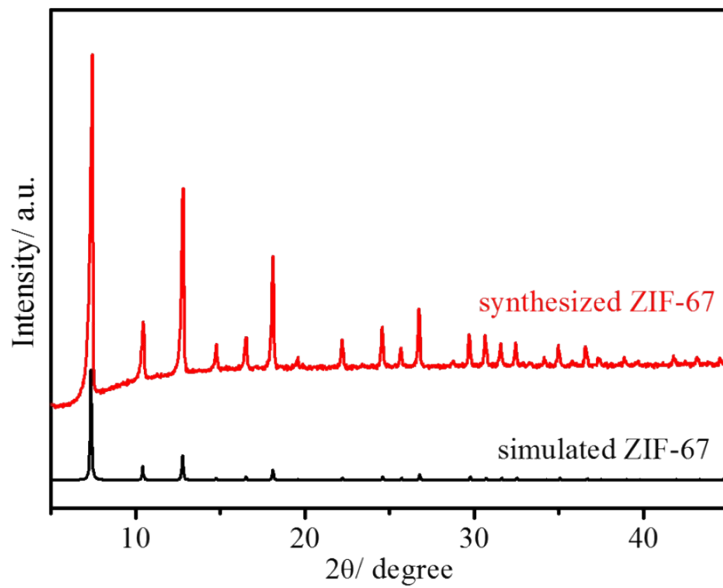
Fig. S1. XRD patterns of as-synthesized ZIF-67 and simulated ZIF-67.
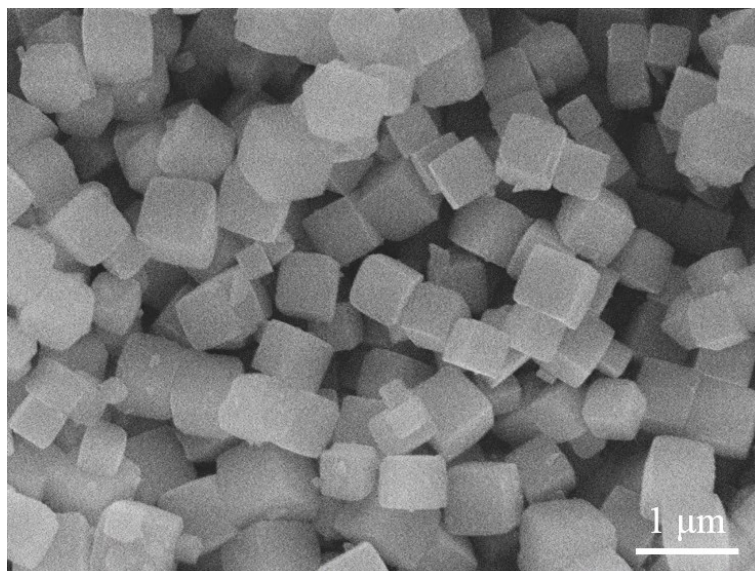

Fig. S2. SEM image of the as-synthesized ZIF-67.
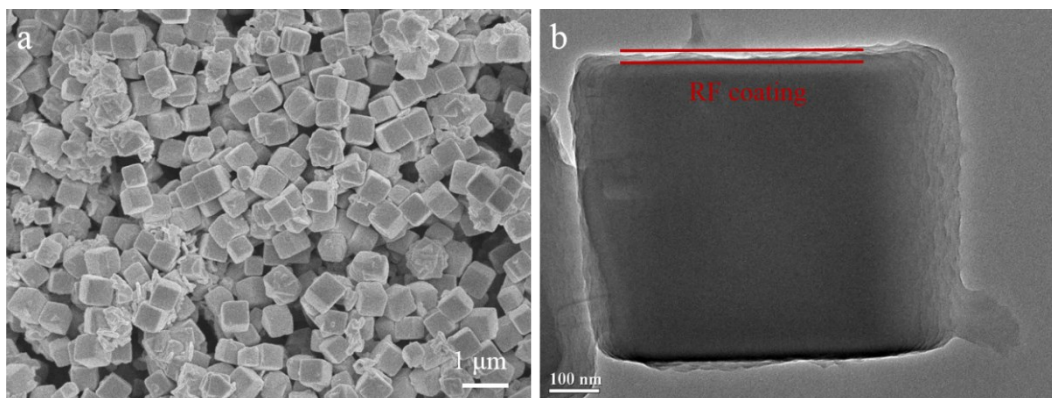
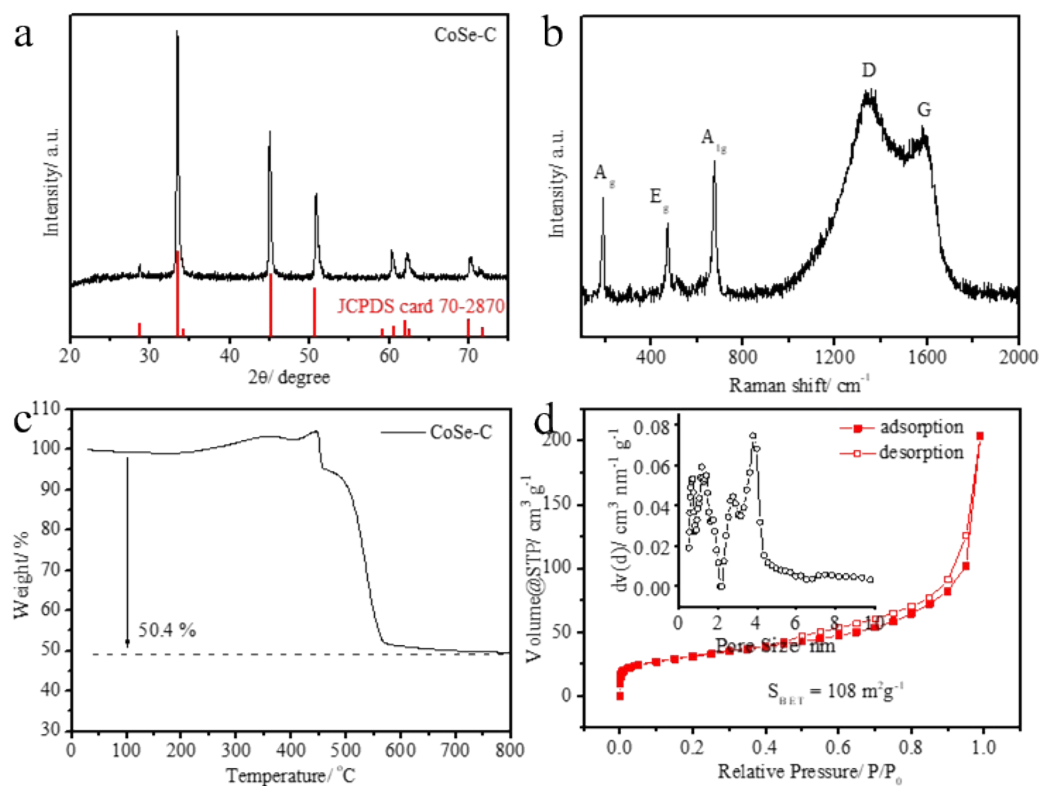**Fig. S3.** (a) SEM image and (b) TEM image of as-synthesized ZIF-67@RF.

Fig. S4. (a) XRD pattern and (b) Raman spectrum of CoSe-C. (c) TGA curve of CoSe-C

tested from room temperature to 800 $^\circ$C in air at a heating rate of 10 $^\circ$C min^{-1}. (d) N$_2$

adsorption/desorption isotherm of CoSe-C obtained at 77 K.
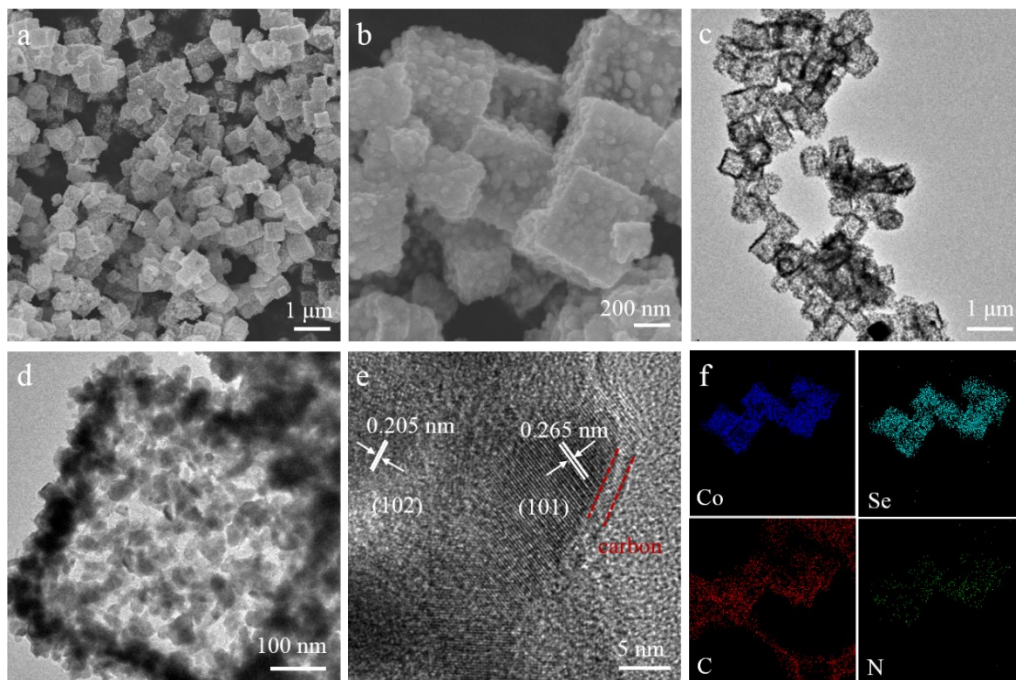
Fig. S5. (a, b) SEM images, (c, d) low-resolution TEM images, (e) high-resolution TEM image, and (f) EDS element mapping images of CoSe-C.
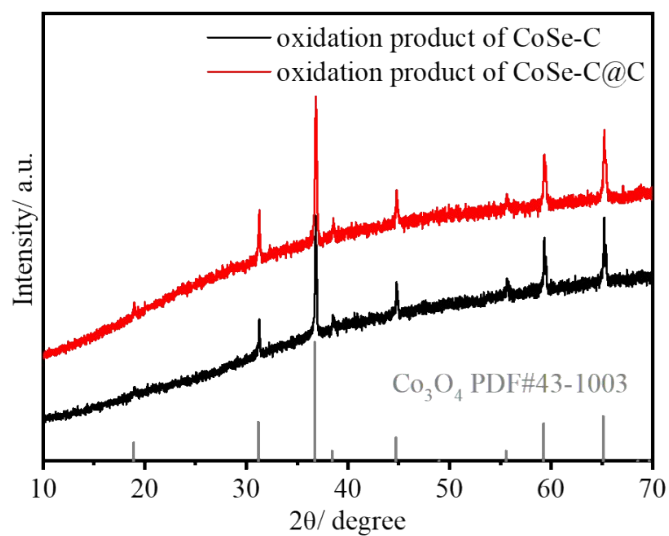

Fig. S6. XRD patterns of the products obtained by the annealing of CoSe-C and CoSe-C@C at 800 ^{o}C in air with a heating rate of 10 ^{o}C min^{-1}.
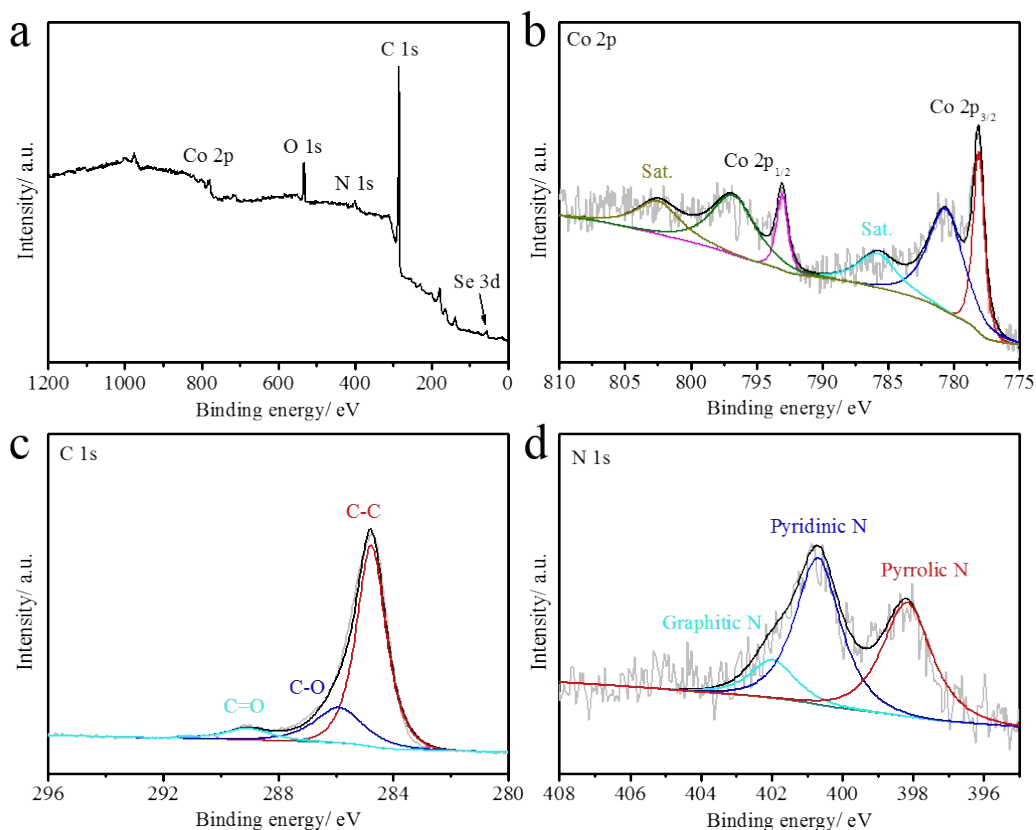
Fig. S7. Surface composition and chemical states of various elements in CoSe-C@C. (a) XPS survey spectrum, and (b) Co 2p, (c) C 1s, and (d) N 1s spectra.

XPS measurements were further carried out to study the surface characteristics of CoSe-C@C, as shown in Fig. S7. The XPS survey spectrum (Fig. S7a) confirms that the chemical constitution is composed of Co, Se, C, and N elements in CoSe-C@C, which is consistent with the EDS results. In the high-resolution Co 2p spectrum (Fig. S7b), two chemical states, Co $2p_{3/2}$ and Co $2p_{1/2}$, as well as two satellite peaks, are detected. The peaks at the binding energies of 780.7 eV for Co $2p_{3/2}$ and 796.7 eV for Co $2p_{1/2}$ can be attributed to the Co^{2+} in CoSe (*ACS Appl. Mater. Inter.* **2017,** *9*, 3624-3633). The peaks at 778.1 eV

for Co 2p$_{3/2}$ and 793.1 eV for Co 2p$_{1/2}$ demonstrate the presence of metallic Co, which may be owing to incomplete selenization of the Co species (*ACS Appl. Mater. Inter.* **2017, 9**, 3624-3633; *Chem. Eur. J.* **2016, 22**, 4140-4146; *Nano Energy* **2018, 53**, 524-535). The high-resolution C 1s spectrum (Fig. S7c) can be fitted into three peaks at 284.8, 286.0, and 289.1 eV, which could be ascribed to the contributions of C–C, C–O, and C=O, respectively (*Adv. Mater.* **2018, 30**, 1800804). The high-resolution N 1s spectrum (Fig. S7d) presents three peaks centred at 398.2, 400.7, and 402.3 eV, corresponding to pyridinic-N, pyrrolic-N, and graphitic-N, respectively (*J. Mater. Chem. A* **2018, 6**, 17959-17966).
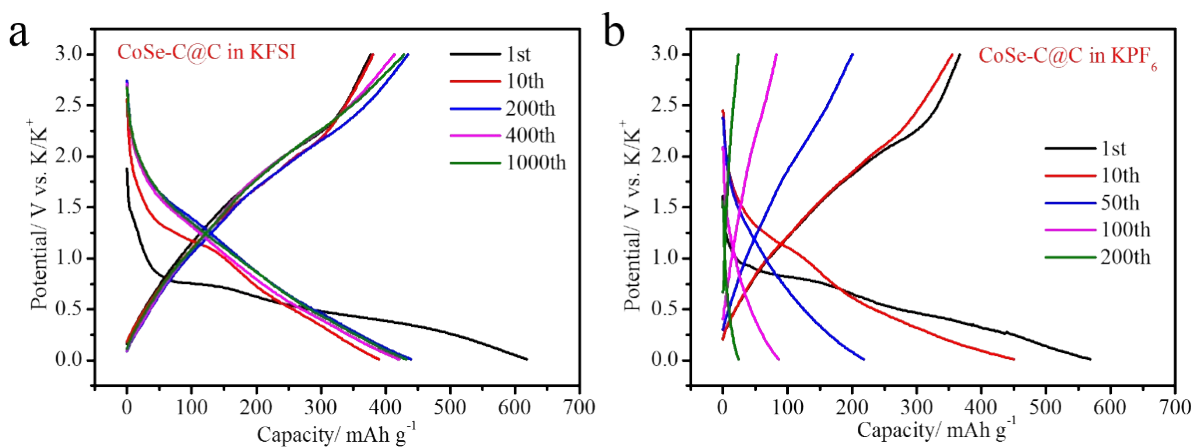

Fig. S8. Galvanostatic discharge/charge profiles of CoSe-C@C electrode at 200 mA g^{-1} in (a) KFSI and (b) KPF$_6$ electrolytes.
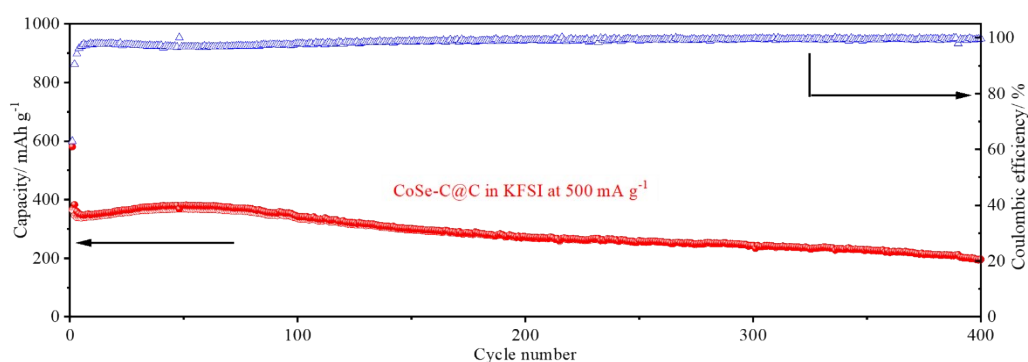
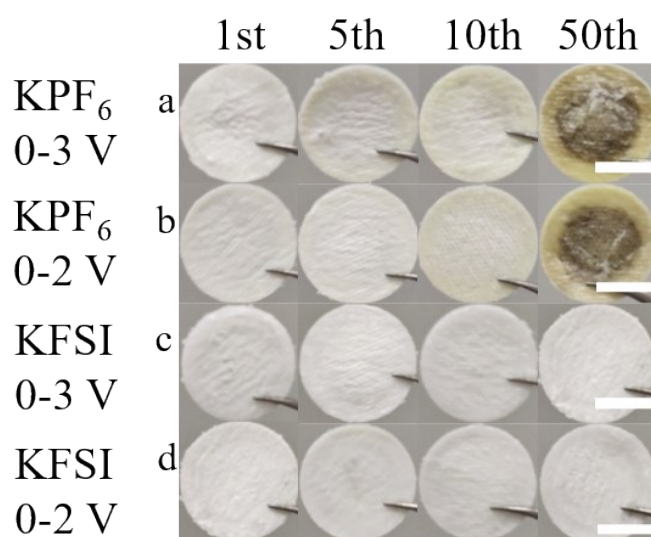**Fig. S9.** Cycling performance of CoSe-C@C electrode at 500 mAh g^{-1}.

Fig. S10. Digital photographs of separators after different numbers of cycles in (a) KPF$_6$

electrolyte in a voltage window of 0-3 V, (b) KPF$_6$ electrolyte in 0-2 V, (c) KFSI

electrolyte in 0-3 V, and (d) KFSI electrolyte in 0-2 V. Scale bar is 9.5 mm.

The separator in KFSI electrolyte retains its integrity with no color changes after cycling.

Whereas, the separator in KPF$_6$ electrolyte turns yellowish after cycling, indicating that the

electrolyte was being decomposed. In addition, in KPF$_6$ electrolyte, the active material peels off

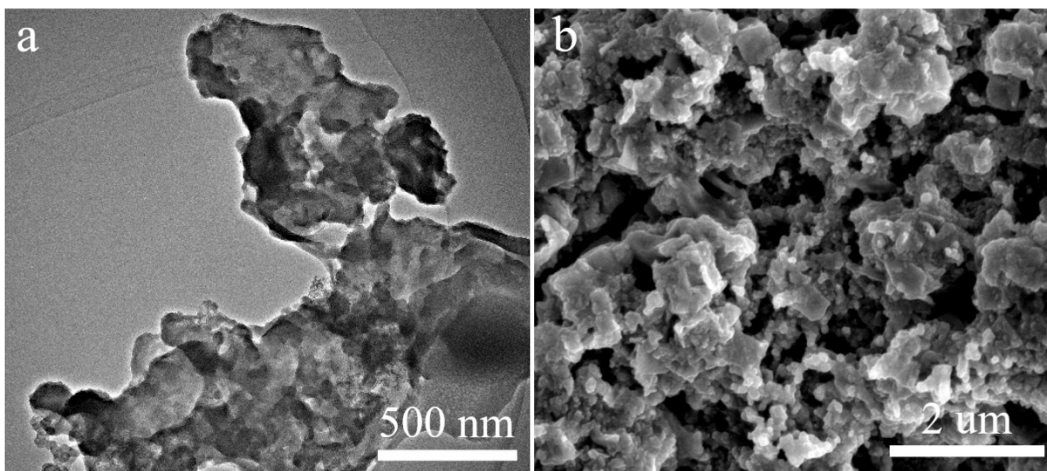from the current collector and merges into the separator after 50 cycles.

Fig. S11. TEM and SEM images of CoSe-C electrode in KFSI electrolyte after 50 cycles.
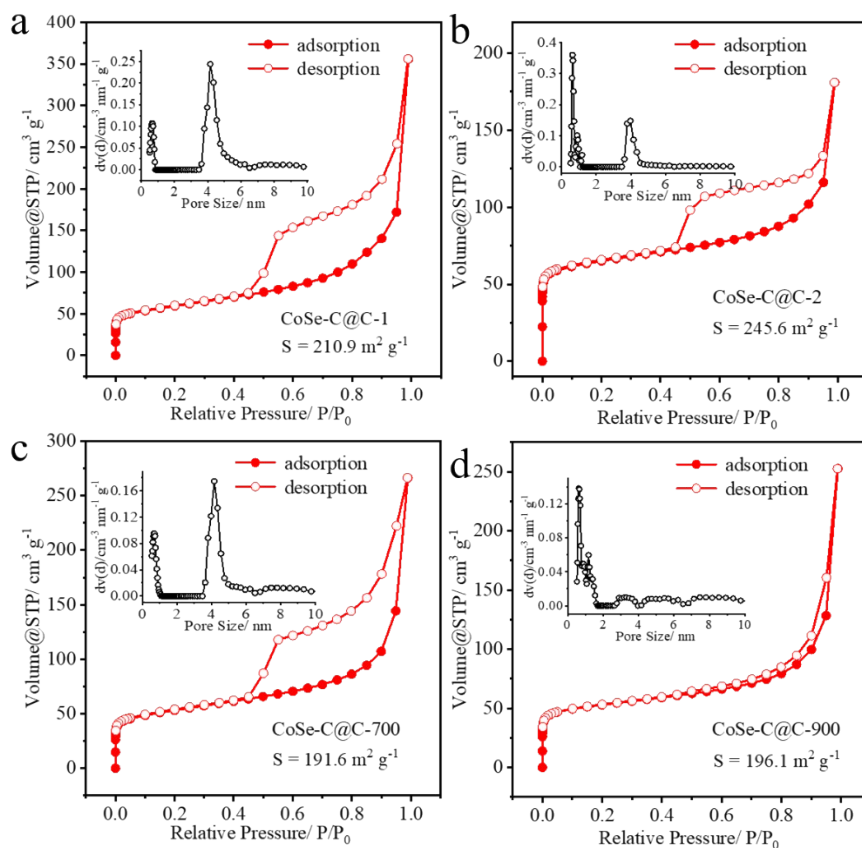

Fig. S12. N$_2$ sorption isotherms and pore size distribution curves (insets) of (a) CoSe-C@C-1, (b) CoSe-C@C-2, (c) CoSe-C@C-700, and (d) CoSe-C@C-900.
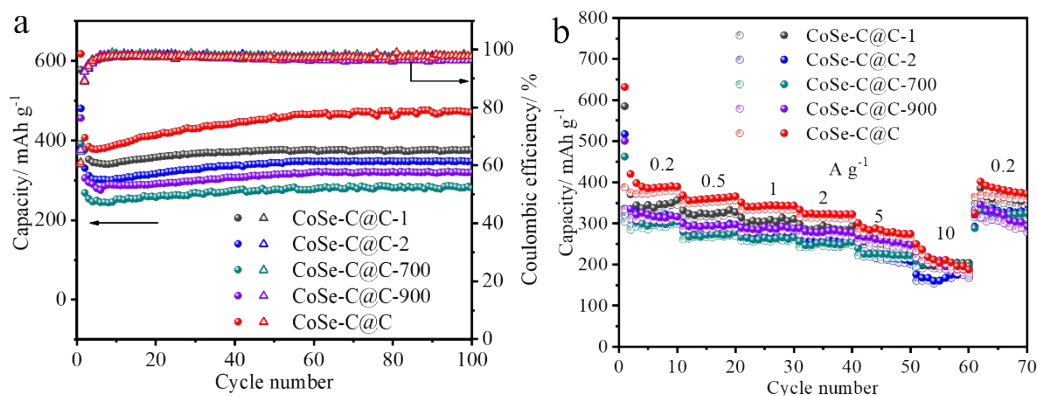
Fig. S13. (a) Cycling performance of CoSe-C@C-1, CoSe-C@C-2, CoSe-C@C-700, CoSe-C@C-900, and CoSe-C@C at 200 mA g^{-1} in KFSI electrolyte, and the corresponding Coulombic efficiencies. (b) Rate performance of CoSe-C@C-1, CoSe-C@C-2, CoSe-C@C-700, CoSe-C@C-900, and CoSe-C@C in KFSI electrolyte.
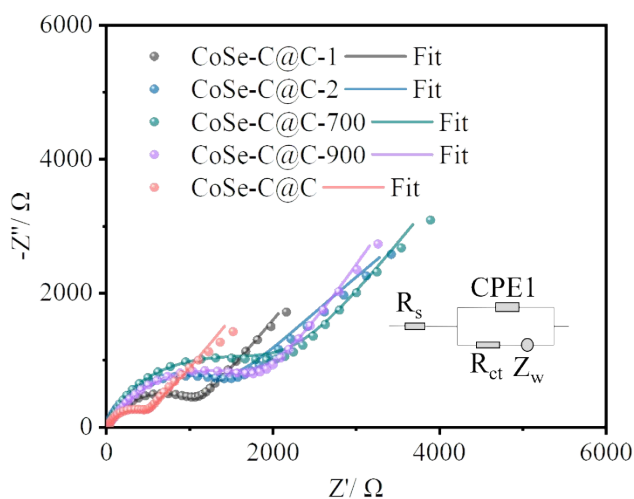

Fig. S14. Nyquist plots and equivalent circuit of CoSe-C@C-1, CoSe-C@C-2, CoSe-C@C-700, CoSe-C@C-900, and CoSe-C@C in KFSI electrolyte after 10 activation cycles.
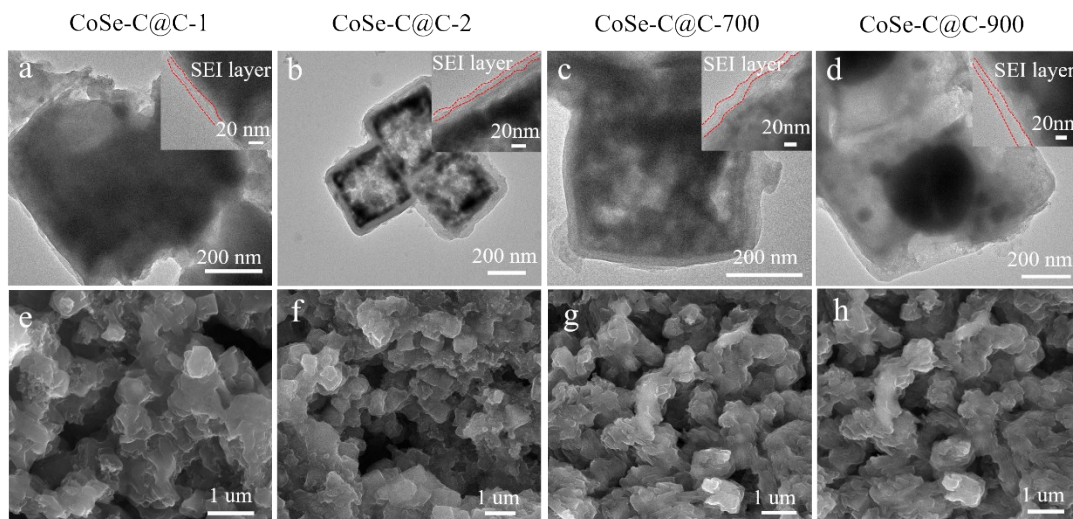
Fig. S15. *Ex-situ* TEM images and SEM images of (a, e) CoSe-C@C-1, (b, f) CoSe-C@C-2, (c, g) CoSe-C@C-700, and (d, h) CoSe-C@C-900 in KFSI electrolyte after 50 cycles with enlargements in the insets.
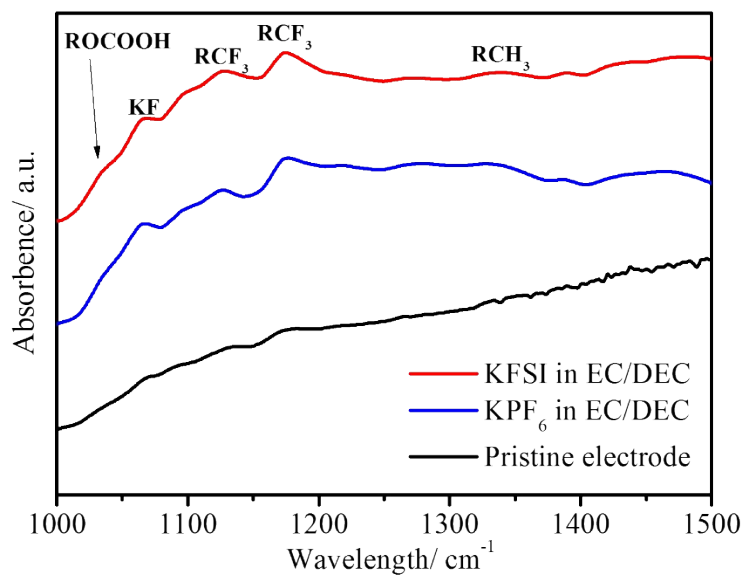

Fig. S16. FTIR spectra of the CoSe-C@C electrode in KFSI and KPF_6 electrolytes after 10 activation cycles.
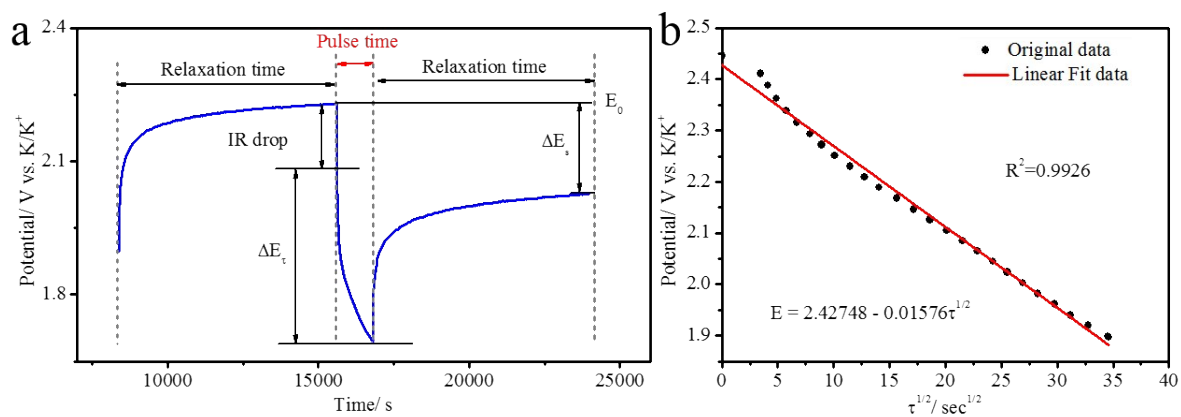
Fig. S17. (a) Time vs. voltage profile of CoSe-C@C electrode in KFSI electrolyte for a single GITT process. The current pulse lasted 20 min, followed by two hours of relaxation time to reach the steady state. (b) Linear behavior of the potential E *vs.* $\tau^{1/2}$ relationship, where τ is the current pulse time.
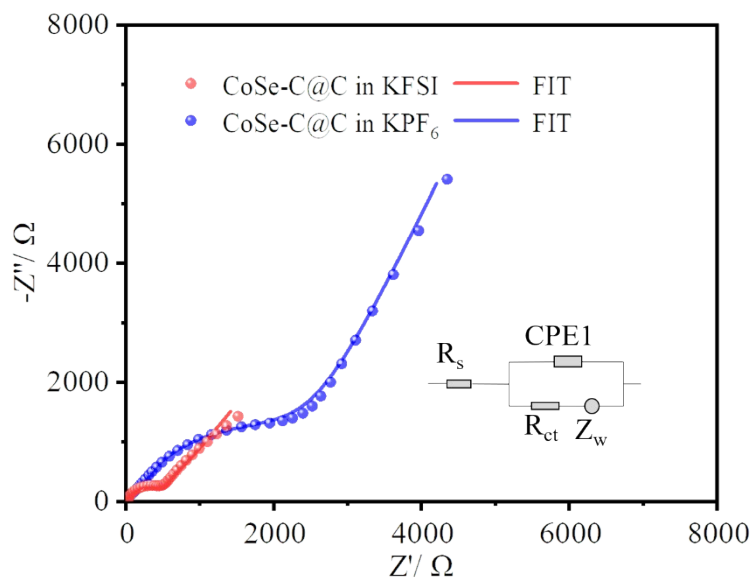
Fig. S18. Nyquist plots and equivalent circuit of the CoSe-C@C electrode in KFSI and KPF$_6$ electrolytes after 10 activation cycles.

15

Fig. S19. Quantitative analysis of capacitive K storage and diffusion-controlled K storage of CoSe-C@C electrode in KPF$_6$ electrolyte. (a) CV curves of CoSe-C@C electrode at scan rates of 0.2-1.0 mV s^{-1}. (b) *b* value determination. (c) Contributions of capacitive K storage and diffusion-controlled K storage at various scan rates. (d) Contribution of capacitive K storage at the scan rate of 1.0 mV s^{-1}.
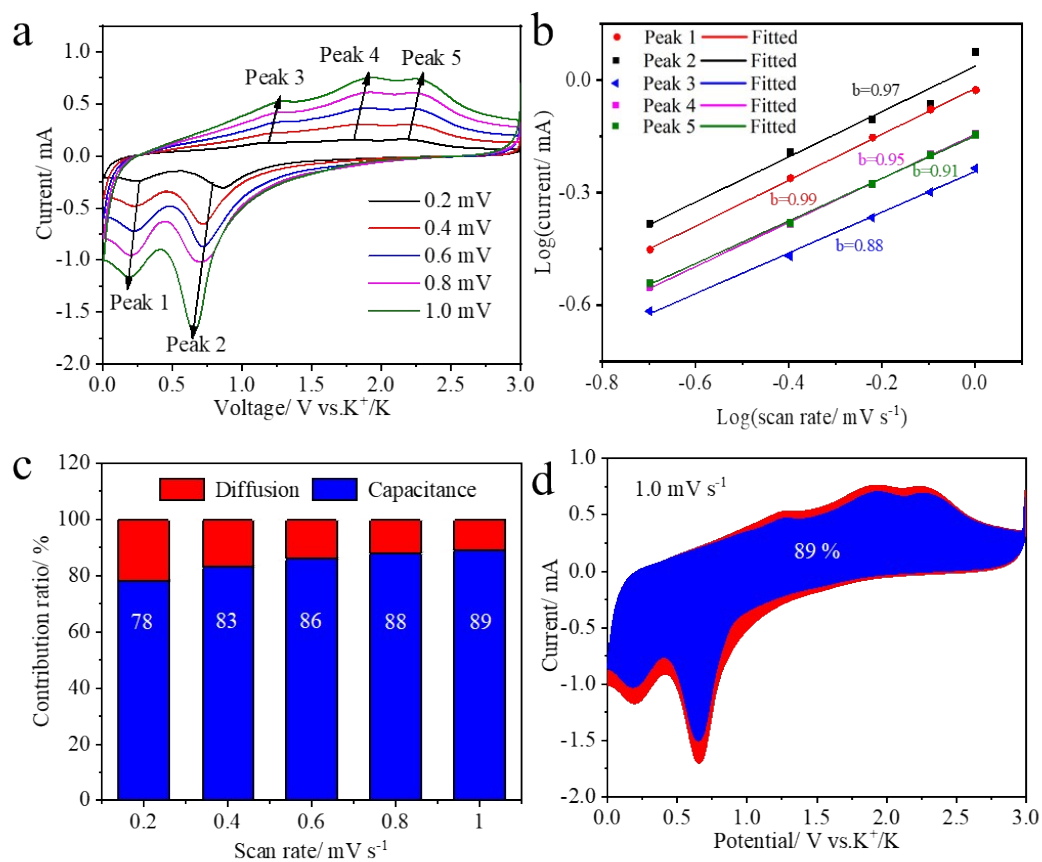
Fig. S20. Quantitative analysis of capacitive K storage and diffusion-controlled K storage of

CoSe-C electrode in KFSI electrolyte. (a) CV curves of CoSe-C electrode at scan rates of 0.2-1.0

mV s^{-1}. (b) *b* value determination. (c) Contributions of capacitive K storage and diffusion-

controlled K storage at various scan rates. (d) Contribution of capacitive K storage at the scan
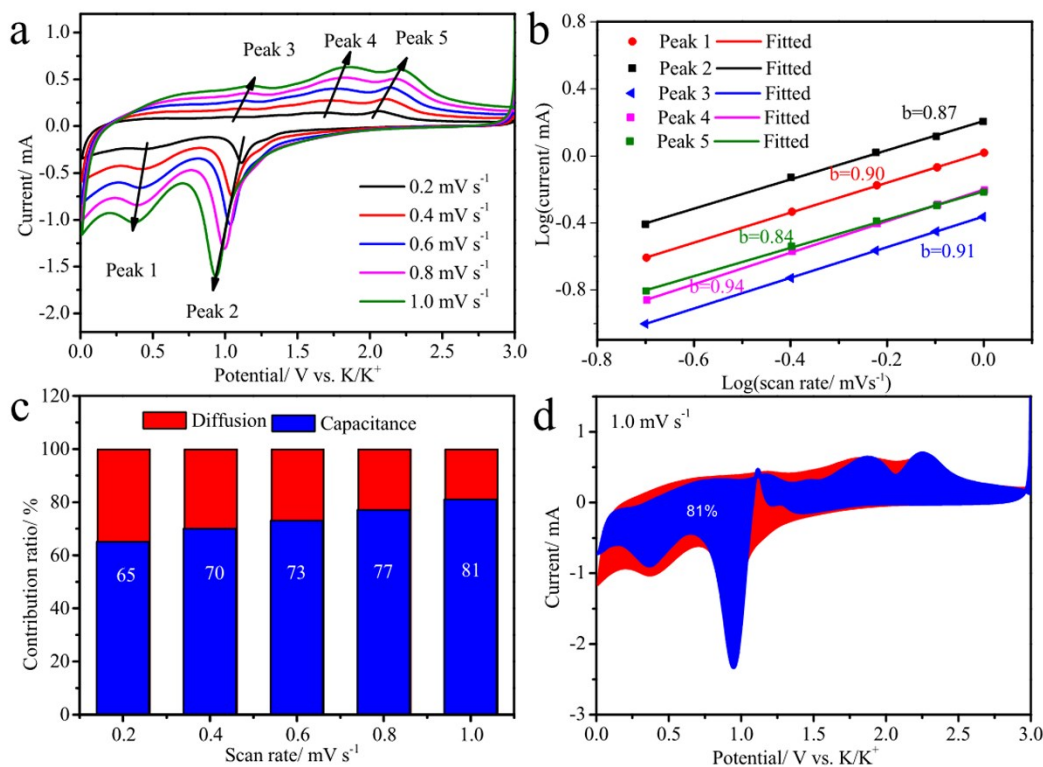
rate of 1.0 mV s^{-1}.

Fig. S21. Quantitative analysis of capacitive K storage and diffusion-controlled K storage of CoSe-C electrode in KPF$_6$ electrolyte. (a) CV curves of CoSe-C electrode at scan rates of 0.2-1.0 mV s^{-1}. (b) *b* value determination. (c) Contributions of capacitive K storage and diffusion-controlled K storage at various scan rates. (d) Contribution of capacitive K storage at the scan rate of 1.0 mV s^{-1}.
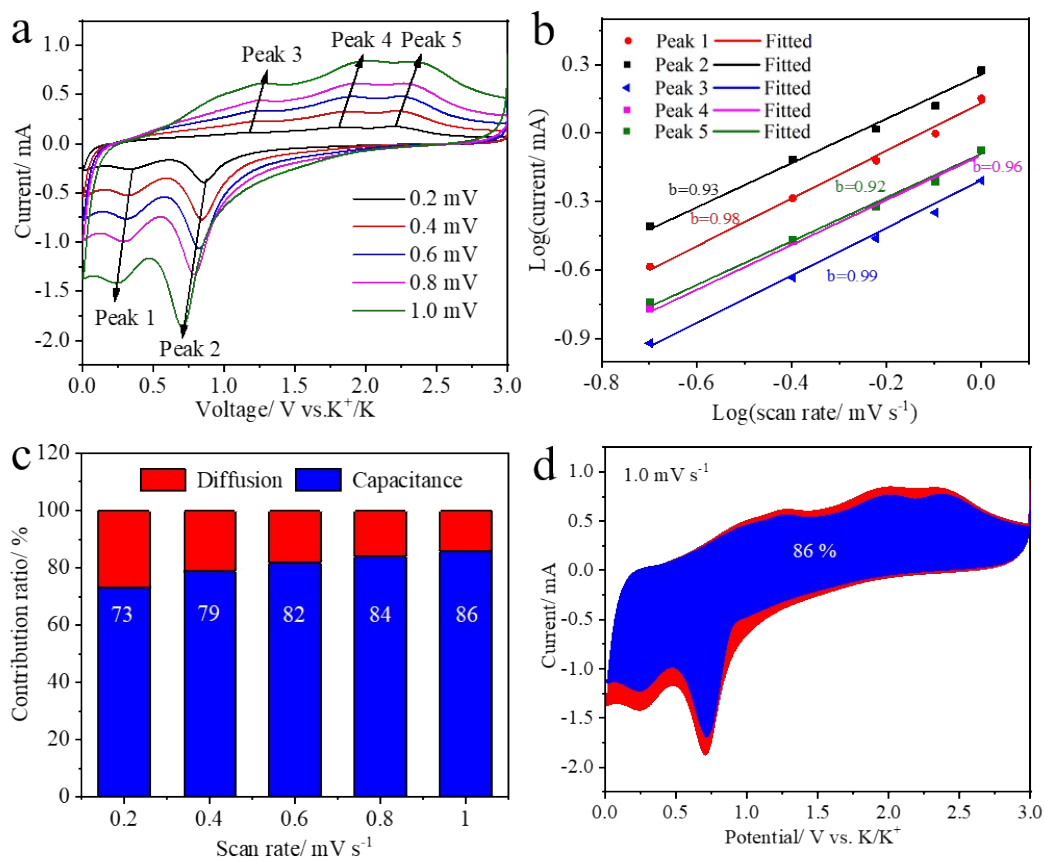
Table S1. Conversion and alloying materials for PIBs.

Anode material	Reversible capacity (mAh g^{-1})@cycle number	Current density (mA g^{-1})	Reference
CoSe-C@C	432@1000	200	This work
MoSe$_2$/N-C	258@300	100	[1]
MoSe$_2$/C	322@100	200	[2]
CoSe$_2$/N-C	253@100	200	[3]
VSe$_2$	335@200	200	[4]
FeMoSe$_4$@N-C	298@100	200	[5]
MoSe$_2$/Mxene/C	335@100	200	[6]
Sb$_2$Se$_3$@C	313@40	100	[7]
Se/C	396@100	200	[8]
FeS$_2$@C	308@100	300	[9]
CoS@G	311@100	500	[10]
VS$_2$ nanosheet	360@100	500	[11]
MoS$_2$/N-C	212@200	100	[12]
Sb$_2$S$_3$/C	404@200	500	[13]
Sn$_4$P$_3$@C	403@200	50	[14]
Sn/C	276@100	50	[15]
Sb/C	551@100	100	[16]
Nanoporous Sb	318@50	100	[17]
Bi@N-C	268@100	1000	[18]
Red P@N-C	650@100	100	[19]

1.   Ge, J.; Fan, L.; Wang, J.; Zhang, Q.; Liu, Z.; Zhang, E.; Liu, Q.; Yu, X.; Lu, B. MoSe$_2$/N-Doped Carbon as Anodes for Potassium-Ion Batteries. *Adv. Energy Mater.* **2018,** *8*, 1801477.

2.   Wang, W.; Jiang, B.; Qian, C.; Lv, F.; Feng, J.; Zhou, J.; Wang, K.; Yang, C.; Yang, Y.; Guo, S. Pistachio-Shuck-Like MoSe$_2$/C Core/Shell Nanostructures for High-Performance Potassium-Ion Storage. *Adv. Mater.* **2018,** *30*, 1801812.

3.   Yu, Q.; Jiang, B.; Hu, J.; Lao, C.-Y.; Gao, Y.; Li, P.; Liu, Z.; Suo, G.; He, D.; Wang, W.; Yin, G. Metallic Octahedral CoSe$_2$ Threaded by N-Doped Carbon Nanotubes: A Flexible Framework for High-Performance Potassium-Ion Batteries. *Adv. Sci.* **2018,** *5*, 1800782.

4.   Yang, C.; Feng, J.; Lv, F.; Zhou, J.; Lin, C.; Wang, K.; Zhang, Y.; Yang, Y.; Wang, W.; Li, J.; Guo, S. Metallic Graphene-Like VSe$_2$ Ultrathin Nanosheets: Superior Potassium-Ion Storage and Their Working Mechanism. *Adv. Mater.* **2018,** *30*, 1800036.

5.   Chu, J.; Yu, Q.; Yang, D.; Xing, L.; Lao, C.-Y.; Wang, M.; Han, K.; Liu, Z.; Zhang, L.; Du, W. Thickness-control of ultrathin bimetallic Fe-Mo selenide@N-doped carbon core/shell

"nano-crisps" for high-performance potassium-ion batteries. *Appl. Mater. Today* **2018,** *13*, 344-351.

6.   Huang, H.; Cui, J.; Liu, G.; Bi, R.; Zhang, L. Carbon-Coated MoSe$_2$/MXene Hybrid Nanosheets for Superior Potassium Storage. *ACS Nano* **2019,** *13*, 3448-3456.

7.   Yi, Z.; Qian, Y.; Tian, J.; Shen, K.; Lin, N.; Qian, Y. Self-templating growth of Sb$_2$Se$_3$@C microtube: A convention-alloying-type anode material for enhanced K-ion batteries. *J. Mater. Chem. A* **2019,** *7*, 12283-12291.

8.   Liu, Y.; Tai, Z.; Zhang, Q.; Wang, H.; Pang, W. K.; Liu, H. K.; Konstantinov, K.; Guo, Z. A new energy storage system: Rechargeable potassium-selenium battery. *Nano Energy* **2017,** *35*, 36-43.

9.   Zhao, Y.; Zhu, J.; Ong, S. J. H.; Yao, Q.; Shi, X.; Hou, K.; Xu, Z. J.; Guan, L. High-Rate and Ultralong Cycle-Life Potassium Ion Batteries Enabled by In Situ Engineering of Yolk-Shell FeS$_2$@C Structure on Graphene Matrix. *Adv. Energy Mater.* **2018,** *8*, 1802565.

10. Gao, H.; Zhou, T.; Zheng, Y.; Zhang, Q.; Liu, Y.; Chen, J.; Liu, H.; Guo, Z. CoS quantum dot nanoclusters for high-energy potassium-ion batteries. *Adv. Funct. Mater.* **2017,** *27*, 1702634.

11. Zhou, J.; Wang, L.; Yang, M.; Wu, J.; Chen, F.; Huang, W.; Han, N.; Ye, H.; Zhao, F.; Li, Y. Hierarchical VS$_2$ nanosheet assemblies: A universal host material for the reversible storage of alkali metal ions. *Adv. Mater.* **2017,** *29*, 1702061.

12. Jia, B.; Yu, Q.; Zhao, Y.; Qin, M.; Wang, W.; Liu, Z.; Lao, C. Y.; Liu, Y.; Wu, H.; Zhang, Z. Bamboo-Like Hollow Tubes with MoS$_2$/N-Doped-C Interfaces Boost Potassium-Ion Storage. *Adv. Funct. Mater.* **2018,** *28*, 1803409.

13. Liu, Y.; Tai, Z.; Zhang, J.; Pang, W. K.; Zhang, Q.; Feng, H.; Konstantinov, K.; Guo, Z.; Liu, H. K. Boosting potassium-ion batteries by few-layered composite anodes prepared via solution-triggered one-step shear exfoliation. *Nat. Commun.* **2018,** *9*, 3645.

14. Zhang, W.; Pang, W. K.; Sencadas, V.; Guo, Z. Understanding high-energy-density Sn$_4$P$_3$ anodes for potassium-ion batteries. *Joule* **2018,** *2*, 1534-1547.

15. Huang, K.; Xing, Z.; Wang, L.; Wu, X.; Zhao, W.; Qi, X.; Wang, H.; Ju, Z. Direct synthesis of 3D hierarchically porous carbon/Sn composites via in situ generated NaCl crystals as templates for potassium-ion batteries anode. *J. Mater. Chem. A* **2018,** *6*, 434-442.

16. Zheng, J.; Yang, Y.; Fan, X.; Ji, G.; Ji, X.; Wang, H.; Hou, S.; Zachariah, M. R.; Wang, C. Extremely stable antimony–carbon composite anodes for potassium-ion batteries. *Energy Environ. Sci.* **2019,** *12*, 615-623.

17. An, Y.; Tian, Y.; Ci, L.; Xiong, S.; Feng, J.; Qian, Y. Micron-Sized Nanoporous Antimony with Tunable Porosity for High-Performance Potassium-Ion Batteries. *ACS Nano* **2018,** *12*, 12932-12940.

18. Yang, H.; Xu, R.; Yao, Y.; Ye, S.; Zhou, X.; Yu, Y. Multicore-Shell Bi@N-doped Carbon Nanospheres for High Power Density and Long Cycle Life Sodium-and Potassium-Ion Anodes. *Adv. Funct. Mater.* **2019,** *29*, 1809195.

19. Wu, Y.; Hu, S.; Xu, R.; Wang, J.; Peng, Z.; Zhang, Q.; Yu, Y. Boosting potassium-ion battery performance by encapsulating red phosphorus in free-standing nitrogen-doped porous

hollow carbon nanofibers. *Nano Lett.* **2019,** *19,* 1351-1358.

Table S2. Calculated results of potassium salts and solvents by DFT.

	LUMO（eV）	HOMO（eV）
DEC	0.065091104	-6.417378748
EC	-0.206022052	-6.873288596
KPF$_6$	-3.371376316	-6.211383908
KFSI	-4.864253848	-6.24052796